FLIGHT DYNAMIC MODELING AND STABILITY OF A SMALL-SCALE SIDE-BY-SIDE HELICOPTER FOR URBAN AIR MOBILITY

Francesco Mazzeo, University of Modena and Reggio Emilia, Modena (MO), Italy

Daniele Fattizzo, University of Bologna, Forlì (FC), Italy

Giulia Bertolani, University of Bologna, Forlì (FC), Italy

Emanuele L. de Angelis, University of Bologna, Forlì (FC), Italy

Fabrizio Giulietti, University of Bologna, Forlì (FC), Italy

Francesco Leali, University of Modena and Reggio Emilia, Modena (MO), Italy

Marilena D. Pavel, Delft University of Technology, The Netherlands

Abstract

In the present paper, a numerical analysis of the flight dynamics of a small-scale side-by-side helicopter is presented. The aim is to study the trim and stability characteristics of a first prototype dual-rotor VTOL by employing iterative procedures and a suitable modeling approach. According to the trim conditions, the design and control mix allow for piloting the rotorcraft as a classical helicopter, using collective pitch and longitudinal/lateral cyclic controls to move forward and laterally. The stability analysis highlights a few criticalities related to the rotors configuration and center of mass position. Nevertheless, the configuration turns out to be a good candidate for future services in urban air mobility ecosystem. The original contribution of the paper is represented by the modeling framework adopted for the analysis and the particular case studied. Indeed, the presence of the shrouds and the constructive design of this rotorcraft make its level of societal acceptance higher than classical VTOLs.

Keywords

Flight Dynamics, helicopter, side-by-side, Urban Air Mobility, stability , trim

1. INTRODUCTION

In 2022, the transport industry was responsible for more than 20% of the global greenhouse gas emissions, whose majority can be related to road transport and aviation sectors (2022 IEA report [1], [2]). The alarming increase of CO_2 production in the last decades has led to the definition of innovative, green-oriented, transport solutions. Urban Air Mobility (UAM) is an example of a sustainable industry sector with has solidly grown in the last few years with the aim of moving part of classical urban and regional transport into the third dimension [3]. The introduction of a UAM ecosystem in modern societies would be determinant for the reduction of traffic congestion, greenhouse gas emissions, and travel time [4]–[6]. The main characters of UAM are the Vertical Take-Off and Landing (VTOL) aircraft, whose capacities make them suitable to carry on services like air taxi, last-mile delivery, rescue, and emergency transportation within urban and regional environments. A large variety of VTOL configurations has been designed and investigated in order to find the most suitable arrangement for particular scenarios. Silva and Johnson proposed different performance studies and sizing methodologies for VTOLs within urban and regional missions [7] [8], setting the stage for future developments of each configuration. The well-known and certainly one of the most established VTOL configurations is the multirotor. The simplicity of the design and the control through rotors RPM of these rotorcraft make them suitable to perform UAM services such as cargo, last-mile delivery, monitoring and surveillance [9]–[11]. This configuration presents a high hovering efficiency to the detriment of bad cruising capabilities [12], making the achievable maximum range quite limited. On the other hand, tilt-rotors [13]–[16] and lift+cruise [17] present a promising solution to increase the cruise efficiency of multirotor, by employing fixed-wing technologies when traveling in forward flight and converting into multirotor for vertical flight operations. Nevertheless, being most of the UAM scenarios foreseen within urban and regional environments, a compromise between the already mentioned configurations had to be found. A widely investigated solution is the dual rotor configuration, both developed in a tandem and side-by-side arrangement [18]. One of the most famous rotorcraft of this category is the Boeing CH-47 Chinhook developed in the 60s for the U.S. Army. Several studies can be found in the literature related to this vehicle, both from an experimental, by employing small-scale models [19]–[21], and a numerical point of view. Cao *et al.* [22] performed a stability and controllability analysis by employing open-loop flight dynamic models based on momentum and vortex theories, comparing the results with experimental data and validating the model. On the other hand, Stengel *et al*. [23] proposed a digital flight control system for the same rotorcraft and studied the closed-loop dynamics with variable gain scheduling. Similarly, Dzul *et al*. [24] presented a Lyapunov control algorithm for tandem helicopters by using backstepping techniques. Both the controllers worked well for the analyzed configuration, providing insights about the handling a controllability quality of the rotorcrafts. Although this configuration is highly accepted as a good candidate for a wide range of operations, it is known that it presents some criticalities related to the stability and aerodynamic properties of the two rotors. According to Newman [25], the presence of aft and rear rotors may induce potential mode couplings between longitudinal and lateral dynamics that can be detrimental to the controllability of the rotorcraft. In addition, when the rotorcraft assumes a nose-up attitude, the rear rotor may operate directly in the downwash of the aft one and induce pitch instability. A solution to overcome this problem can be found by rearranging the rotors side-by-side, with the longitudinal axis perpendicular to the rotor-rotor one. The rotorcraft would have two counter-rotating main rotors, as the tandem does, and thus no need for an anti-torque system placed in the tail. The lateral and yaw dynamics would be similar to the longitudinal and yaw ones of the tandem configuration, while it can operate as a single-rotor aircraft in vertical and longitudinal motions [18], [25]. A dynamic model of a side-by-side helicopter was presented by Rao *et al*. [26] together with a control system designed by employing Hamilton's principle to reduce the torque oscillations. In their analysis, the feedback control manages to stabilize the rotorcraft even if the angle and torque transients remain quite evident. A potential drawback of this configuration is the noise generated by the aerodynamic interaction of the rotors with the fuselage and the rotors themselves. Indeed, most of the side-by-side helicopters studied in the literature, present two overlapped and intermeshing rotors being this arrangement more efficient than two isolated rotors and thus beneficial for the overall performance of the helicopter [27]. An acoustic prediction of the background noise generated by side-by-side rotors in hovering conditions, with different levels of overlap, was conducted by Sagaga *et al*. [28] by employing CFD simulations. It was found that the noise level, which is mainly related to the tip vortex interactions between the two rotors, can be decreased by reducing the level of overlap between the two rotors. Nevertheless, the rumor intensity still remained above the maximum threshold set by Uber for air taxi services in a UAM ecosystem (67 dB at 500 ft altitude [29]). Yunus *et al.* [30] and Barbarino *et al.* [31] presented two aeroacoustic simulations of eVTOL operating within vertiport and urban environments, studying the noise level introduced by the rotorcraft in strategic locations of a UAM ecosystem. It is indeed of primary importance to assess the disturbance level of this particular configuration in order to be able to consider the side-by-side helicopter a potential candidate for future services. Considering the level of societal acceptance in UAM is fundamental and requires additional studies and the introduction of innovative solutions [32].

In this paper, a particular type of side-by-side helicopter is presented and studied. The rotorcraft has two ducted rotors placed outside of the fuselage's boundary, with zero overlap and negligible aerodynamic interaction with the airframe. The presence of the ducts makes the rotorcraft very suitable to operate within urban environments, increases the level of safety and societal acceptance, and has a very low effect on the overall noise [27]. While the majority of the research efforts have been focused on alternative configurations or acoustic predictions of the side-by-side helicopter noise, very small knowledge is still present on the flight dynamic properties of this particular configuration. The aim of this paper is thus to fill in this gap by developing a numerical model to assess the stability and handling qualities of the above-mentioned small-scale eVTOL. The goal is to propose this rotorcraft as a candidate for future UAM services such as cargo and air taxi in urban environments. The remainder of the paper is organized as follows: in Section 2 the case study is presented and a description of the particular configuration and controlling methods is given.

Section 3 is devoted to describing the modeling framework used to study the stability and dynamic properties of the rotorcraft: in particular, Section 3.2 describes the main rotor model, while Section 3.3 presents the correction used to take the shroud effects into account and Section 3.4 describes how the fuselage loads are estimated. In Section 4, the equilibrium conditions of the rotorcraft are investigated by employing an iterative algorithm, while in Section 5, the linearized dynamic model is developed and the main modes presented. Finally, in Section 6 the main outcomes from this study are presented and discussed while Section 7 follows with the concluding remarks.

2. DESIGN OVERVIEW

The case study is a small-scale electric dual-rotor VTOL configuration produced by SAB Group S.R.L. The rotorcraft is made of two identical semi-rigid helicopter rotors arranged side-by-side and connected by a carbon fiber beam, with no incidence angle with respect to the rotorcraft's body axes. The fuselage is a lightweight carbon fiber structure, symmetric with respect to the plane $x_B - z_B$, and designed to allocate two 22000 mAh Li-Po batteries underneath. Two custom-made electric motors are placed at the very end parts of the upper beam. The shrouded rotors are synchronous and counter rotating and they operate at constant angular speed. Figure 1 illustrates the design, while the technical specifications are reported in Table 1. In particular, the main rotor 1 (MR1) is referred to as the right-hand side clockwise rotor, while the main rotor 2 (MR2) is referred to as the left-hand side counterclockwise rotor.

Figure 1: Electric dual-rotor VTOL configuration, courtesy of SAB Group S.R.L.

Description	Symbols	Values
Maximum take-off mass [kg]	m_{to}	20.620
Inertia moment wrt x_B[kgm^2]	I_{xx}	3.532
Inertia moment wrt y_B[kgm^2]	I_{yy}	2.222
Inertia moment wrt z_B[kgm^2]	I_{zz}	5.342
Inertia moment wrt x_B[kgm^2]	I_{yz}	0
Inertia moment wrt y_B[kgm^2]	I_{xz}	-0.052
Inertia moment wrt z_B[kgm^2]	I_{xy}	-0.001
Rotors (same design, counter rotating)		
Sense of rotation	Γ	±1
Number of blades	N_b	3
Radius [m]	R	0.505
Mean Chord [m]	c	0.051
Solidity ratio [-]	σ	0.0964
Angular velocity [rpm]	ω	2400
Hinge offset [m]	e	0.075
Blade mass [kg]	m_b	0.2875
Spring restraint coefficient due to flap [Nm/rad]	K_b	162.69
Pitch-flap coupling ratio	K_1	0
Precone angle [rad]	a_0	0
Hub position of the MR1 wrt body axes (x, y, z)	$r_H^{(1)}$	0 -0.645 0.066
Hub position of the MR2 wrt body axes (x, y, z)	$r_H^{(2)}$	0 0.645 0.066

Table 1: Rotorcraft technical specifications. The body axes system $[x_B\ y_B\ z_B]$ is referred to as a right-handed axes system, with the origin in the rotorcraft center of gravity, the x_B pointing towards the nose of the vehicle and the y_B pointing towards the right hand side main rotor.

Each rotor is equipped by the classical helicopter controls, i.e. collective ($\theta_0^{(1,2)}$), lateral cyclic ($B_{1s}^{(1,2)}$) and longitudinal cyclic ($A_{1s}^{(1,2)}$), where the superscripts $^{(1)}$ and $^{(2)}$ refer respectively to the main rotor 1 and main rotor 2. The rotorcraft is thus over-actuated, meaning that the set of six controls requires to be mixed in order to reduce it to four global controls [33]. The global collective pitch (θ_0) is used to control the vehicle along the vertical axis, while global lateral and longitudinal cyclic (A_{1s} and B_{1s}) allows for controlling the roll and pitch attitude. The heading angle control, which is generally performed by the tail rotor, is introduced by a differential longitudinal cyclic ΔB_{1s} which generates a yawing moment about the vertical axis. Lateral and forward movements are performed with a simultaneous modification of the single longitudinal and lateral controls, as well as the collective pitch which is kept equal in the two rotors. To summarize

(1) $$\theta_0 = \theta_0^{(1)} = \theta_0^{(2)} \quad , \quad A_{1s} = A_{1s}^{(1)} = A_{1s}^{(2)}$$

(2) $$B_{1s} = \frac{B_{1s}^{(1)}+B_{1s}^{(2)}}{2} \quad and \quad \Delta B_{1s} = \frac{B_{1s}^{(2)}-B_{1s}^{(1)}}{2}$$

In such a way, the rotorcraft can be piloted as a normal small-scale helicopter, but without the need for a tail rotor to counteract the main rotor torque and introduce a yawing moment.

3. SIMULATION MODEL

3.1. Overview of the simulation model

The mathematical model of the dual-rotor VTOL is a nonlinear model with 12 degrees of freedom: six for the rigid body motion and six for the rotor flapping (3 for each rotor). The rotor angular velocity is kept constant and its dynamic is neglected. The lead-lag dynamics are neglected as well, as their effects on the rotorcraft trim and stability are of secondary importance. The single elements of the model are reported in the block diagram in Figure 2.

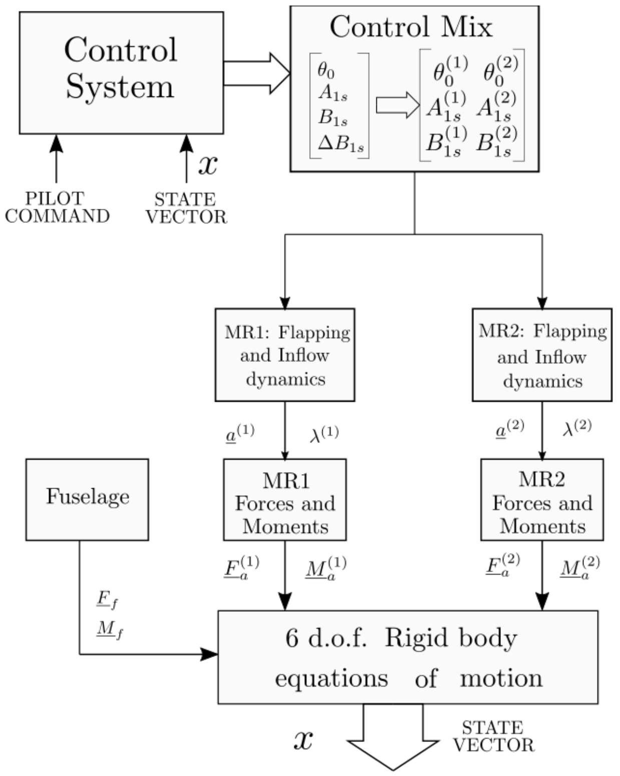

Figure 2: Scheme of the simulation model

3.2. Main Rotor

The two main rotors are modeled as semi-rigid ones, according to the mathematical framework developed by Talbot [34]. The same modeling approach is applied for both of the rotors, with the only difference related to the hub position with respect to the rotorcraft's center of mass and the rotor sense of rotation. For the sake of simplicity, in this section, the framework is presented for a generic rotor, while in the following ones, the two rotors will be differentiated by a superscript (1) and (2). The blades are assumed to be rigid and their forces and moments are integrated along the blade span to obtain an analytical expression of the loads in the local hub-body frames. The latter is defined as a frame of reference with the origin located in the rotor's center of rotation and the x_H and z_H axes respectively perpendicular and parallel to the shaft. In particular, while the expression of these forces can be found in [34], a correction for the clockwise rotor is applied according to Choi *et al.* [35]. The correction involves the use of symmetrical, local hub-body coordinate systems for the two rotors, thus a right-handed one for the counter-clockwise rotor ($\Gamma = 1$) and a left-handed one for the clockwise rotor ($\Gamma = -1$), as depicted in Figure 3. According to this correction, the velocities in hub-body frames for a generic rotor can be expressed as (considering that no incidence is applied to the rotors)

(3) $$\underline{\omega_H} = \begin{bmatrix} \Gamma & 0 & 0 \\ 0 & 1 & 0 \\ 0 & 0 & \Gamma \end{bmatrix} \underline{\omega_B} \quad ,$$

(4) $$\underline{U_H} = \begin{bmatrix} 1 & 0 & 0 \\ 0 & \Gamma & 0 \\ 0 & 0 & 1 \end{bmatrix} \underline{U_B} + \underline{\omega_H} \times \underline{r_H}$$

where $\underline{\omega_H}$, $\underline{\omega_B}$, $\underline{U_H}$, $\underline{U_B}$ are, respectively, the angular velocity and relative wind velocity expressed in local hub-body (subscript H) and body frames (subscript B). The lateral cyclic control input has to be corrected as well when expressed in the hub-body frame as

(5) $$A_{1s}|_H = \Gamma A_{1s}|_B$$

Finally, the aerodynamic forces and moments expressed in body axes ($\underline{F_a}$ and $\underline{M_a}$) for a generic rotor can be found as

(6) $$\underline{F_a} = \begin{bmatrix} \cos\beta_w & \sin\beta_w & 0 \\ -\Gamma \sin\beta_w & \Gamma\cos\beta_w & 0 \\ 0 & 0 & 1 \end{bmatrix} \begin{bmatrix} -H_w \\ Y_w \\ -T_r \end{bmatrix}$$

$$(7)\quad \underline{M_a} = \begin{bmatrix} \Gamma\cos\beta_w & \Gamma\sin\beta_w & 0 \\ -\sin\beta_w & \cos\beta_w & 0 \\ 0 & 0 & \Gamma \end{bmatrix} \begin{bmatrix} L_w \\ M_w \\ Q \end{bmatrix} + \underline{r_H} \times \underline{F_a}$$

where the expression of the horizontal force H_w, lateral force Y_w, rotor thrust T_r, rolling moment L_w, pitching moment M_w and torque Q can be found in Talbot [34]. β_w represents the sideslip angle of the rotor, computed as $\beta_w = \mathrm{atan}_2(v_H, u_H)$, while u_H, v_H, and w_H are the components of U_H.

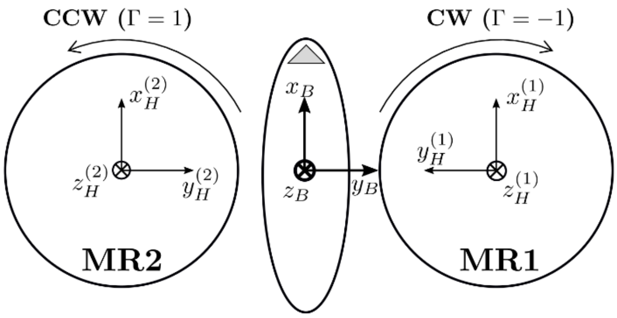

Figure 3: Rotorcraft coordinate system

The mathematical model of the main rotor includes a uniform, nonlinear, induced inflow ratio (λ_i) model derived from general momentum theory [36]. In particular

$$(8)\qquad \dot{\lambda}_i = \frac{3\pi}{4}\left(\frac{C_T}{2} - \lambda_i\sqrt{\mu^2 + \lambda^2}\right)$$

$$\text{where}\quad \begin{cases} \lambda_i = \lambda - \dfrac{w_H}{\Omega R} \\ \mu = \dfrac{\sqrt{u_H^2 + v_H^2}}{\Omega R} \\ C_T = \dfrac{T_r}{\rho A (\Omega R)^2} \end{cases}$$

ρ is the air density, A is the rotor disk area, C_T is the rotor thrust coefficient and λ represents the inflow ratio. The uniform, time-dependent, rotor-induced velocity is defined as

$$v_i = \left(\frac{w_H}{\Omega R} - \lambda\right)\Omega R$$

The blade flapping motion is governed by the tip-path plane dynamic equation presented by Chen [37], [38] for nonteetering rotors. In particular

$$(9)\quad \underline{\ddot{a}} + \widetilde{D}\underline{\dot{a}} + \widetilde{K}\underline{a} = \tilde{f} \quad \textit{where} \quad \underline{a} = [\beta_0\ \ \beta_1\ \ \beta_2]$$

and matrixes $\widetilde{D}$, $\widetilde{K}$ and $\tilde{f}$ can be found in the reference. The blade flapping is thus approximated by the first harmonic terms with time-varying coefficients as

$$(10)\quad \beta(t) = \beta_0(t) - \beta_1(t)\cos\psi_b - \beta_2\sin\psi_b$$

where ψ_b is the azimuthal position of the blade.

For the sake of simplicity, a linear lift coefficient curve is adopted for the simulation at low angles of attack (α). However, a correction factor k_{C_L} is added to take into account blade stall effects, in order to provide more realistic results when the incidence of the blade profile overcomes the maximum lift condition. In particular, look up tables [39] of a *NACA0015* airfoil are employed to evaluate the average (from a Reynolds number point of view) C_{L_α} and stall lift and drag coefficient C_{L_s} and C_{D_s}. In particular the values $C_{L_\alpha} = 4.54$, $C_{L_s} = 1.12$ and $C_{D_s} = 0.052$ are used. Figure 4 shows the lift curve in a range of α between -12° and 90°. It is noticeable that the slope remains constant until the C_L approaches its maximum value, while, above this limit, the lift follows the analytical, approximate, expression proposed by Viterna [40] for post-stall regions. In particular, being α_s the average stall angle and C_{L_α} the curve slope in the pre-stall regime,

$$(11)\qquad C_L = k_{C_L} C_{L_\alpha}\alpha$$

$$\text{where}\quad k_{C_L} = \begin{cases} 1 & if\ \alpha < \alpha_s \\ \dfrac{1}{C_{L_\alpha}}\dfrac{dC_L}{d\alpha} & if\ \alpha > \alpha_s \end{cases}$$

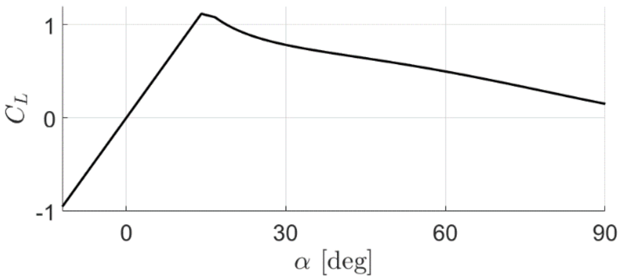

Figure 4: C_L curve NACA0015 with Viterna correction

3.3. Shroud Modeling

The effect of the shroud is taken into consideration as well, by extending the momentum theory to the analysis of a ducted fan. Theoretical analysis conducted by Kruger [41] has shown that the presence of a shroud may be beneficial for the rotor performance, by decreasing the power required to produce the same amount of thrust. By following the approach presented by Leishman [42], the total thrust T produced by the ducted rotor can be computed as the sum of two contributions:

$$(12)\qquad T = T_r + T_d \quad \text{where} \quad \frac{T_d}{T} = 1 - \frac{1}{2a_w}$$

T_r is the thrust produced by the isolated rotor and its expression can be found in Talbot [34]. T_d is instead an additional contribution that arises from the presence of the shroud and depends on the wake contraction factor a_w generated by the geometry of the shroud itself. Estimating a_w has always been a challenging matter from both a numerical and an experimental point of view and different analyses can be found in the literature for improving the accuracy of fan-in-fin tail rotor models or ducted fans [43], [44]. While an extensive aerodynamic study would be required in order to evaluate the interaction between the rotor and the shroud, for the sake of this study an analytical and simpler model is preferred. The semi-analytical mathematical model developed by Bourtsev et al. [45] can be adapted for the present case, as it directly links the duct's geometry to the pressure losses. In particular, a "lip" duct inlet and outlet are considered, with a lip radius (r_k) of 0.01 m and a blade tip clearance (δ) of 0.01 m. The wake contraction factor can be computed as

$$a_w = \frac{1}{2}\left(1 + \delta_f\left[\frac{K_v}{2} + \frac{(\xi_{in}+\xi_{out})}{2K_v} - 1\right]\right)^{-1} \quad (13)$$

$$\text{where} \quad \delta_f = 1 - 109\frac{\delta}{R}\sqrt{\frac{\delta}{R}}$$

δ_f is the blade tip clearance factor, and K_v is the velocity ratio between the inlet and the outlet. ξ_{in} is the inlet drag factor and is evaluated as a function of the lip radius according to the experimental data provided by Bourtsev et al. [45]. The outlet drag factor ξ_{out} is equal to zero.

3.4. Fuselage

A bottleneck of the analysis is the estimation of the fuselage aerodynamic loads. The geometry of the airframe behaves as a bluff body that interferes with the surrounding fluid by creating forces and moments that affect the flight dynamics of the rotorcraft. In this particular case, due to the side-by-side configuration, it can be easily assumed that the fuselage does not interfere with both of the rotor's inflow and the only influence that it has on the dynamics of the rotorcraft comes from the pressure distribution created by the income velocity. As a matter of fact, a complete aerodynamic study, either by employing CFD or wind tunnel experiments, would be required to perfectly model these loads at different velocities and variable orientations. However, this type of investigation is out of the scope of this study and a simpler visualization is preferred. The fuselage is modeled by employing a set of equivalent flat plate areas, each of them with specific parasite drag and surface. The latter hypothesis involves the assumption that the fuselage behaves as a non-lifting body, thus the force generated while moving in the air is only a parasite drag, i.e. directed in the direction of the velocity. The fuselage is approximated as depicted in Figure 5, where the three main flat plates (frontal, top, and side) are characterized by their surface and drag coefficient. The fuselage drag is computed as a sum of the contributions from the three flat plates, which depends on the orientation of the incoming flow. In particular

$$D = D_f + D_s + D_t \quad (14)$$

$$\text{where} \quad \begin{cases} D_f = \frac{1}{2}\rho U_\infty^2 S^f C_D^f(\hat{U}\cdot\hat{x}) \\ D_s = \frac{1}{2}\rho U_\infty^2 S^s C_D^s(\hat{U}\cdot\hat{y}) \\ D_t = \frac{1}{2}\rho U_\infty^2 S^t C_D^t(\hat{U}\cdot\hat{z}) \end{cases}$$

$\hat{x}$, $\hat{y}$ and $\hat{z}$ are the versors perpendicular to the frontal (superscript f), side (superscript s) and top (superscript t) faces, while $\hat{U}$ is the versor parallel to the incoming flow velocity, i.e. $\hat{U} = \underline{U}/U_\infty$ with U_∞ the velocity magnitude. The scalar product between the surface normal and the velocity versor determines the portion of the flat plate invested by the flow. The values of the equivalent surfaces and relative parasite drag coefficients, reported in Table 2, are estimated by using a simplified geometry of the vehicle modeled with OpenVSP (Figure 6).

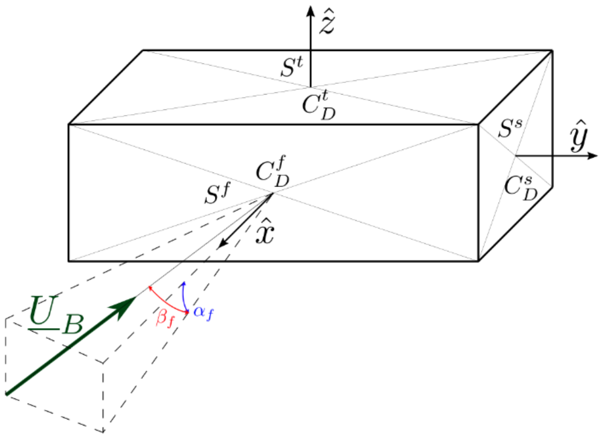

Figure 5: Flat plate approximation for the fuselage aerodynamics

$S^f = 0.3426$ m^2	$C_D^f = 0.3854$
$S^s = 0.2065$ m^2	$C_D^s = 0.6356$
$S^t = 0.8034$ m^2	$C_D^t = 0.1645$

Table 2: Reference surfaces and drag coefficients of the equivalent flat plate fuselage approximation

Estimating the center of pressure (CP) is another important aspect of fuselage modeling. Still, a complete aerodynamic analysis would be needed, but for the sake of this paper and according to the symmetry planes that characterize the vehicle, it is assumed that the aerodynamic force can be applied in front of the CG, along the longitudinal plane. In this way, the fuselage will only contribute with pitching and yawing moments, respectively when different angles of attack and sideslip occur. In particular, the CP is assumed to be placed at 1/3 of the parallelepiped depth, thus 0.26 m in front of the CG. The latter is a general approximation that can be made for flat plates. The forces and moments in body axes can be expressed as

(15) $$\underline{F_f} = -D\underline{\hat{U}} \quad \text{and} \quad \underline{M_f} = \underline{r_{CP}} \times \underline{F_f}$$

where $\underline{r_{CP}}$ is the center of pressure position vector.

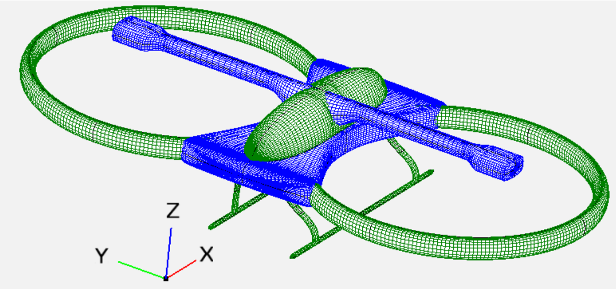

Figure 6: Fuselage modeling in OpenVSP

4. TRIM ROUTINE

An iterative algorithm based on the Newton-Rapson method is implemented in order to compute the trim conditions of the vehicle at different velocities. The trim condition is an equilibrium point at which the rotorcraft maintain the steady-state flight and the sum of the forces and moments acting on it is equal to zero. In order to estimate this condition, a system of 14 unknowns and 14 equations is solved and the following assumptions are made: zero acceleration ($d\underline{U_B} = d\underline{w_B} = 0$), constant rotor angular velocity ($\Omega_1 = \Omega_2 = constant$), yaw angle ψ equal to 0 and constant $\underline{U_B}$ and $\underline{w_B}$. The system of equations to be solved is the following:

(16) $$\begin{cases} \left[\tilde{K}\underline{a} - \tilde{f}\right]^{(1)} = 0 \\ \left[\tilde{K}\underline{a} - \tilde{f}\right]^{(2)} = 0 \\ \underline{F_{tot}} = \underline{F_a}^{(1)} + \underline{F_a}^{(2)} + \underline{F_g} + \underline{F_i} + \underline{F_f} = 0 \\ \underline{M_{tot}} = \underline{M_a}^{(1)} + \underline{M_a}^{(2)} + \underline{M_i} + \underline{M_f} = 0 \\ A_{1s}^{(1)} = A_{1s}^{(2)} \\ \theta_0^{(1)} = \theta_0^{(2)} \end{cases}$$

and the vector of unknowns is

(17) $$\left[\beta_0^{(1)}\ \beta_1^{(1)}\ \beta_2^{(1)}\ \beta_0^{(2)}\ \beta_1^{(2)}\ \beta_2^{(2)}\ \theta_0^{(1)} \ldots \right.$$
$$\left. \ldots\ A_{1s}^{(1)}\ B_{1s}^{(1)}\ \theta_0^{(2)}\ A_{1s}^{(2)}\ B_{1s}^{(2)}\ \theta\ \phi\right]$$

where the superscripts $^{(1)}$ and $^{(2)}$ indicate the main rotor 1 and main rotor 2 while θ and ϕ are the attitude pitch and roll angles. The same modeling approach described in Section 3 is applied for both of the rotors. The first six equations of the system are the flapping dynamics (Equation (9)) in steady condition for the two rotors, thus by imposing $\underline{\ddot{a}}$ and $\underline{\dot{a}}$ equal to zero. The second six are the total force and moment acting on the rotorcraft. In particular, while $\underline{F_a}$, $\underline{M_a}$, $\underline{F_f}$ and $\underline{M_f}$ have already been presented in sections 3.2 and 3.4, the gravitational force $\underline{F_g}$ and inertial force and moment, $\underline{F_i}$ and $\underline{M_i}$ can be computed as

(18) $$\underline{F_g} = m_{to}\begin{bmatrix} -g\ \sin\theta \\ g\ \sin\phi\cos\theta \\ g\ \cos\phi\cos\theta \end{bmatrix}$$

(19) $$\underline{F_i} = -\left(\underline{\omega_B} \times \underline{U_B}\right)m_{to} \quad , \quad \underline{M_i} = -\underline{\omega_B} \times I\underline{\omega_B}$$

where I is the inertia matrix. The last two equations are additional relations that are added in order to close the system: a constraint on the control mix is set, such that the two rotors operate at the same collective pitch and lateral cyclic, both commanded by the pilot input (see Section 2). Figures 7 and 8 report the results for different forward and lateral speeds.

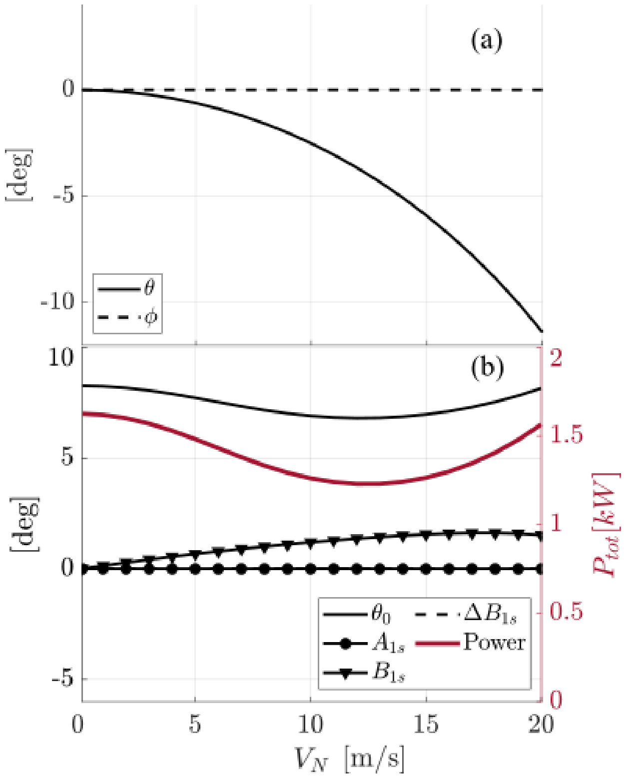

Figure 7: Trim conditions at variable forward speed: rotorcraft attitude (a) and control inputs (b)

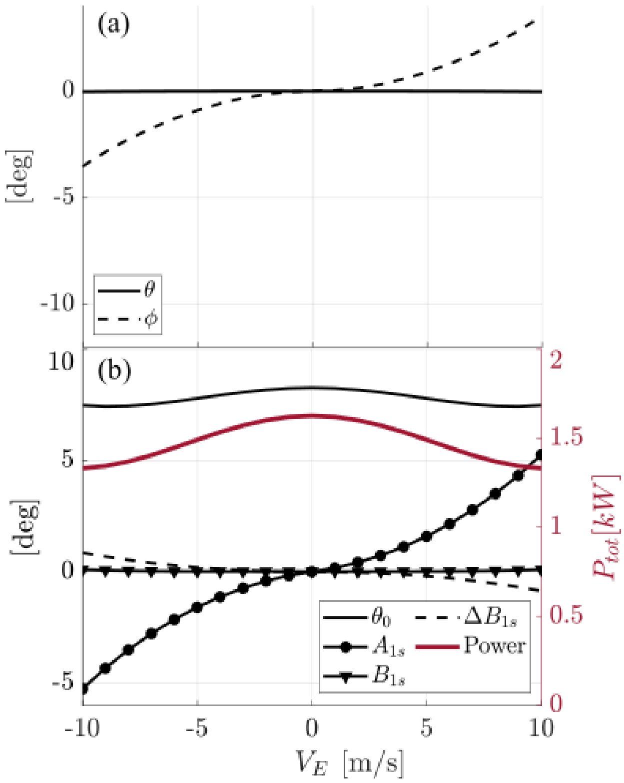

Figure 8: Trim conditions at variable lateral speed: rotorcraft attitude (a) and control inputs (b)

Figure 7 (a) reports the attitude of the rotorcraft at an increasing forward speed. As can be observed, the aircraft pitches down as the speed rises up and to do so a positive longitudinal cyclic B_{1s} is applied (Figure 7 (b)). It has to be reminded that, according to the mathematical model presented in Section 3.2, a positive longitudinal cyclic is intended to be a "push effort" by the pilot, while the attitude signs are defined by the right-handed body axes system. The roll angle ϕ of the rotorcraft remains zero as well as the lateral cyclic effort. Together with the B_{1s}, the collective pitch changes by following the trend of the power. The aircraft absorbs around 1.6 kW in hovering conditions and has a minimum power of 1.2 kW, reached at 12 m/s. As the speed increases, the pitching moment generated by the fuselage becomes stronger due to the higher negative θ and the CP position in front of the CG. The latter produces a decrease of the B_{1s} curve slope, nearly reducing the pilot's effort to maintain the steady condition.

In order to perform a lateral motion, the aircraft rolls in the direction of the speed (ϕ angle in Figure 8 (a)) by following the pilot's lateral cyclic input reported in Figure 8 (b). Together with the A_{1s} control, which is positive in the positive direction of the lateral speed, and the collective pitch, which still follows the power trend, a small contribution of the pedals has to be introduced by the pilot to counteract the yawing moment of the fuselage. Indeed, the $\underline{r}_{CP}$ position in front of the CG generates an unstable moment about the z-axis when the rotorcraft is subjected to a sideslip angle.

5. LINEARIZATION OF THE DYNAMIC MODEL

In order to study the open-loop stability of the dual-rotor configuration, a linear model about a trim condition is developed. The linearized 6 d.o.f. equations of motion are described by the system

$$\dot{x} = Ax + Bu \tag{20}$$

$$\text{where} \quad \begin{cases} x = [u_B \; w_B \; q_B \; \theta \; v_B \; p_B \; \phi \; r_B] \\ u = [\theta_0 \; A_{1s} \; B_{1s} \; \Delta B_{1s}] \end{cases}$$

x and u are the motion state and control vectors, while A and B are the system and control matrices whose expression can be found in Padfield [36]. Note that the heading angle ψ is neglected as it does not affect the dynamics of the rotorcraft. In order to compute the stability derivatives that compose the linear system, a central finite difference formula is applied by perturbing the rotorcraft around a general trim condition. In particular, for a general force/moment F and perturbation dp around the trim state vector x_0, the dimensional linear approximation is computed as

$$\left.\frac{\partial F}{\partial x}\right|_{x_0} = \frac{F(x_0+dp)-F(x_0-dp)}{2dp} \qquad (21)$$

The value of the perturbation is chosen by performing a convergence check on the derivatives in order to not affect their computation. In particular, 10% of the forward velocity is chosen for the forward speed perturbation, 0.1 m/s is used for the other two components while a perturbation of 0.01 rad/s is applied to the angular velocities and 0.1 degrees for the attitude and control angles. The static stability of the system can be assessed by considering the eigenvalues of the state matrix A. In Table 1Table 3, the coupled eigenvalues of the 8 different modes that characterize the rotorcraft rigid body motion are reported in the hovering condition, while Figure 9 reports the set of eigenvectors related to each mode, in a polar representation.

ID	Mode	Eigenvalue	Frequency (rad/s)
1/2	Oscillatory stable	−0.141 ± 0.228i	0.268
3	Unstable real	0.255	0.255
4	Stable real	-0.333	0.333
5/6	Oscillatory stable	−0.125 ± 0.203i	0.2832
7	Unstable real	0.228	0.2683
8	Stable real	-0.000118	0.000118

Table 3: Coupled rigid body motion eigenvalues at hovering

According to the eigenvectors analysis, a first classification can be made between the modes governing the longitudinal and lateral-directional dynamics. As a matter of fact, Table 3 shows the presence of 4 longitudinal modes with similar frequency, where two complex conjugate poles represent an oscillating motion governed by the forward speed u and a complex, small, pitch and heave contribution. These two oscillatory modes can be most likely related to stable phugoid or heave subsidence dynamics. It has to be pointed out that an effort is made to categorize the poles with the classical nomenclature used in conventional aircraft dynamics. Nevertheless, it has to be reminded that, being a totally different design, the case studied may not respond to the same behavior.

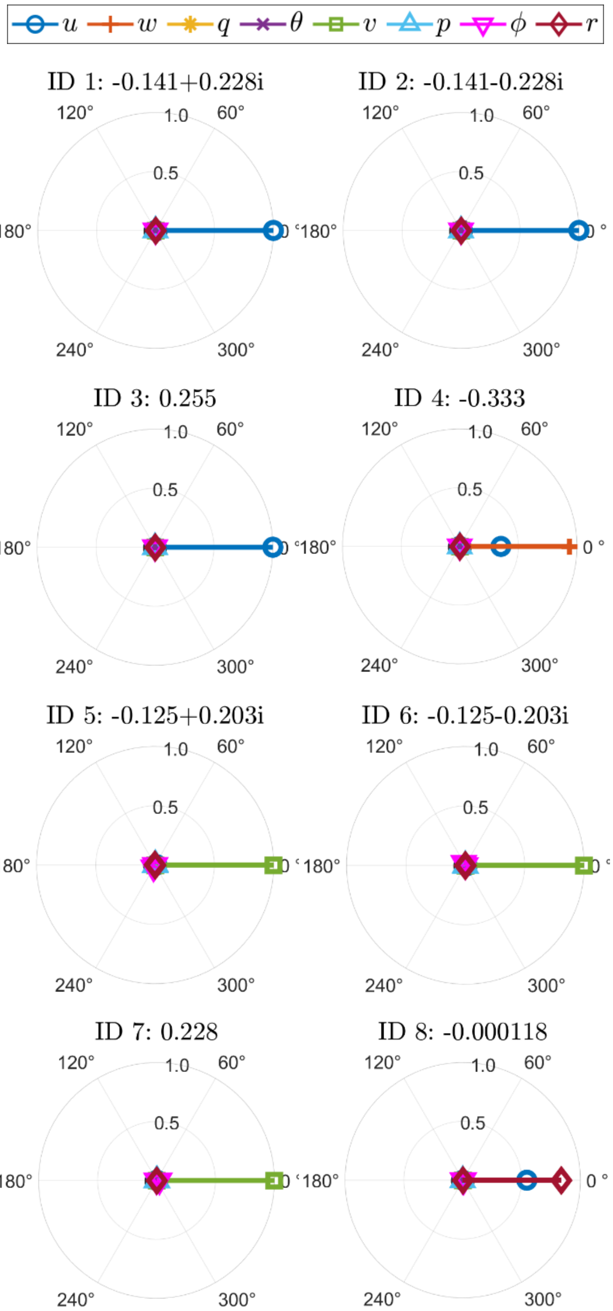

Figure 9: Polar plot of the eigenvectors in hovering conditions

A couple of stable/unstable real poles characterized by a u and w contribution is also present, most likely representing a heave subsidence or short-period dynamics. Indeed, it is still unclear whether these longitudinal poles reproduce the classical modes of conventional aircraft but an extensive analysis will be performed in the next chapter. From the lateral-directional point of view, more classical dutch-roll, roll, and spiral modes will be identified in the following sections. Two stable, complex conjugate poles represent the dutch-roll motion governed by the lateral velocity v, together with an unstable, real and high-frequency, roll pole. Indeed, a very low frequency slightly stable lateral mode can be identified in a yaw subsidence behavior, governed by the directional angular velocity r and forward speed u. It will be observed in Section 6 that this pole will become unstable as the forward speed increases. The latter can be related to the position of the fuselage center of pressure placed in front of the rotorcraft center of gravity.

6. RESULTS

6.1. Variable forward speed dynamics

The linearized model described in Section 5 is used to study the stability of the system in each of its characteristic modes and with an increasing forward speed.

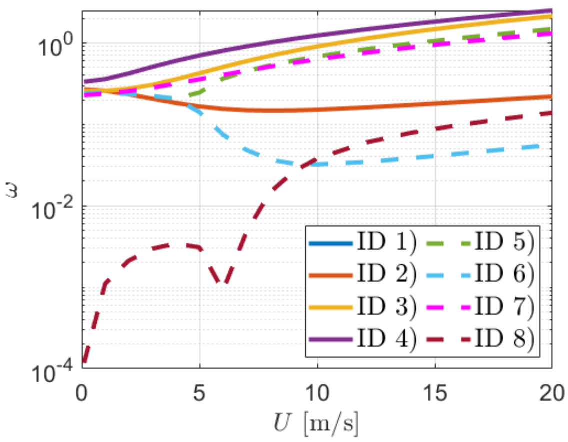

Figure 10: Logarithmic plot of the poles' frequency at variable forward speed

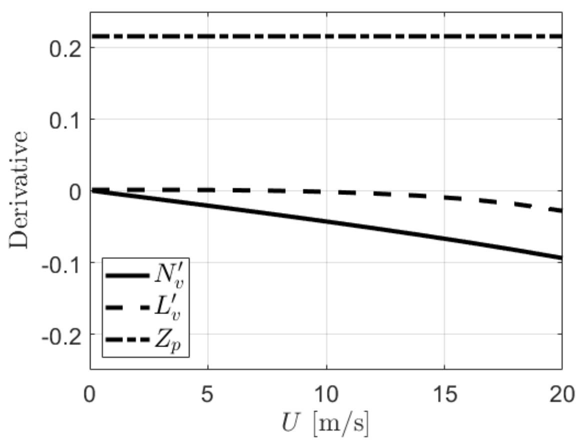

Figure 11: $N_v{}'$ (weathercock stability) and $L_v{}'$ (dihedral effect), and the main coupling derivative Z_p

Figure 14 shows the evolution of the system's poles in a complex plane, while Figure 10 reports their natural frequency in a semi-logarithmic plot. In addition, Figure 15 plots the participation of the 8 modes in each of the rotorcraft poles.

The longitudinal dynamic of the system, i.e. *ID 1, ID 2, ID 3,* and *ID 4*, is characterized by a couple of complex conjugates and two real poles. *ID 1* and *ID 2* represent a low-frequency, oscillatory, dynamics governed by the forward velocity u and a complex contribution of the vertical speed w. The behavior of these poles may be associated with a stable aircraft phugoid/heave subsidence mode. On the other hand, *ID 3* and *ID 4* seem most likely to be related to short-period dynamics, being characterized by a higher frequency and the participation of the pitch angle and pitch rate in Figure 15 that rises as the forward speed increases. The positive one provides a strong longitudinal instability.

By looking at the lateral-directional dynamics, i.e. *ID 5, ID 6, ID 7*, and *ID 8*, a very low frequency, slightly unstable, real pole is present (*ID 8*), representing what is most likely traceable to a spiral mode. The latter is indeed characterized by either the yaw rate and roll angle, together with the forward speed u. *ID 7* is instead a positive real pole which is probably related to an unstable rolling motion governed by the lateral speed. Finally, a couple of complex conjugate poles (*ID 5* and *ID 6*) can be most likely traceable to a stable dutch-roll dynamic, which tends to diverge as the speed increases. It can be observed that these two poles move toward the horizontal axis of the complex plane and become real at around $U = 5$ m/s. Another important aspect of the directional dynamics, is related to the weathercock instability that arises with a negative N_v' and is linked to the fact that the vehicle has basically no stability on the directional axes. As a matter of fact, the CP position in front of the CG and the absence of a vertical fin to damp the yaw rate, make the system directionally unstable.

The only effect of coupling is connected to the derivative Z_p, which is positive and represents the decrease of thrust (opposite to the vertical axis) when the rotorcraft rolls.

6.2. Variable center of gravity dynamics

Additional analysis is performed on the stability of the rotorcraft with a variable CG position. Indeed, the side-by-side helicopter analyzed in this paper allocates the batteries inside the fuselage along its longitudinal axes and the position of the center of gravity can be modified by placing them forward or backward. The analysis presented in Section 6.1 describes the stability of the system with a CG placed on the symmetry plane of the vehicle, which is also aligned with the application of the main rotor force. In the present Section, the CG is shifted along the x-axis of a ΔCG, and the stability is studied. A schematic view of the rotorcraft is reported in Figure 12 to highlight the relative position of these points.

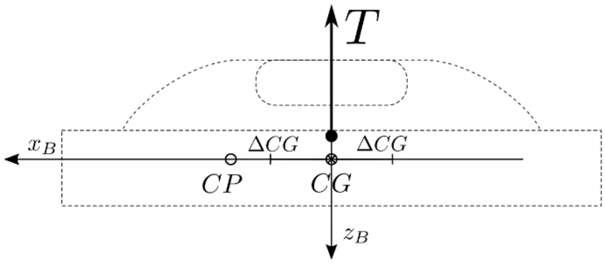

Figure 12: Schematic side representation of the rotorcraft's CG, CP and main rotor force application

Figure 16 reports the evolution of the longitudinal (solid lines) and lateral (dashed lines) poles of the system at $U = 10$ m/s and within an interval of $\Delta CG = \pm 0.2$ m. Figure 17 and Figure 18 report a polar representation of the eigenvectors of the system for two opposite CG positions.

It can be observed that the two longitudinal low-frequency poles (*ID 1* and *ID 2*), identified as a phugoid/heave subsidence mode in the previous Section, become real as soon as the CG is shifted along the x-axis and misaligned with the rotor's arms. Therefore, it can be assumed that the oscillating low-frequency behavior was associated to the vertical alignment between the rotors and the CG. On the other hand, the two poles representing the high-frequency longitudinal dynamics *ID 3* and *ID 4*, associated with a pitch and heave behavior, become negative and oscillatory when the CG is shifted backward, making the system's short period stable.

Concerning lateral stability, it is observed that the position of the center of gravity mostly affects the dutch-roll and the roll poles. While an unstable roll has already been observed in the central CG configuration, the presence of a negative ΔCG can make the dutch-roll poles highly unstable. In particular, placing the CG behind the rotors ($\Delta CG < 0$) can be beneficial for the roll dynamics but drives the dutch-roll towards the positive plane. This can be linked to the evolution of the sideslip derivatives reported in Figure 13, which mainly affect the lateral-directional stability. Indeed, an unstable behavior is connected to negative weathercock stability and a positive dihedral effect, both of them occurring when $\Delta CG < 0$. However, this condition can be improved by installing a properly sized vertical fin, which would increase the directional stability of the system. In this way, the dutch-roll instability can be limited, while the high-frequency longitudinal poles can be stabilized by moving the CG behind the rotor's arms.

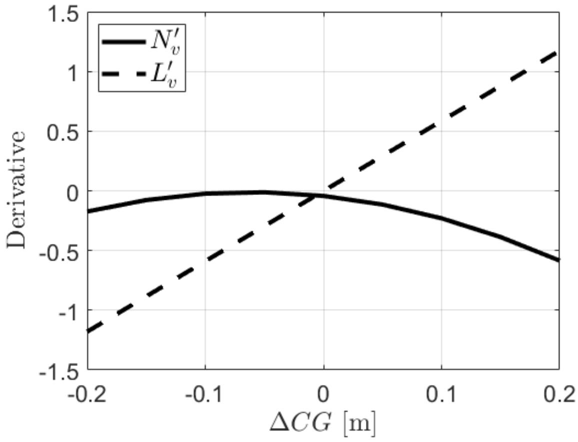

Figure 13: Evolution of the sideslip derivatives N'_v (weathercock stability) and L'_v (dihedral effect) for a variable ΔCG at $U = 10$ m/s.

7. CONCLUSIONS

The analysis presented in this paper has the aim of studying the flight dynamic properties of a small-scale electric dual rotor VTOL for urban air mobility. The configuration proposed in the paper is a side-by-side helicopter, with two identical, shrouded, and counter rotating rotors that operate at constant angular speed. A 12 degrees of freedom nonlinear mathematical model is implemented and improved by considering the effect of the shrouds around the two main rotors and the fuselage aerodynamic loads. The trim conditions of the rotorcraft are evaluated by solving the nonlinear system in steady state conditions: the rotorcraft reaches an equilibrium point for variable forward and lateral speed by employing reasonable ranges of controls and attitude. As a matter of fact, the rotorcraft absorbs 1.6 kW of power to keep the hovering at ground level and applies 8 deg of collective pitch in both of the rotors. A positive longitudinal cyclic, together with a negative pitch angle, is applied to move forward while the lateral cyclic input is used to move laterally and impose a roll angle. The mathematical model is linearized around the above-mentioned trim conditions and a study on the stability characteristics at different speed and CG positions is performed. In particular, an unstable high-frequency mode, governed by the vertical velocity and pitch angle arises when the CG is aligned, or placed in front of the two main rotor's arms. The increase in the forward speed is detrimental to this short-period dynamic. From a lateral – directional stability point of view, it turns out that the spiral mode is unstable for most of the analyzed cases, while the sign of the roll and dutch-roll poles mainly depends on the center of gravity location. In conclusion, the analyzed side-by-side helicopter configuration has the potential to become a good candidate to provide services in a UAM ecosystem, because of its reliable design and societal acceptance. However, the particular case studied in the paper presents some criticalities that need to be solved. In particular, the two main rotors have to be relocated in order to avoid the presence of a center of gravity above the thrust application point. Indeed, in this design, these two locations are almost aligned, causing a strong longitudinal instability. Further, the rotorcraft has almost no directional stability, and the position of the fuselage center of pressures in front of the CG causes a criticality in the yawing motion. A suitable sizing of a vertical fin has to be performed in order to improve the directional damping of the system. Finally, the position of the batteries, originally placed along the longitudinal axes, has to be revised in order to reduce the inertia about the y-axis and possibly move the CG down. As a future work, a CFD analysis of the fuselage will be performed and the "equivalent flat-plate" model substituted with a more reliable one. An experimental campaign on the small-scale prototype is also required in order to validate the numerical results and study the most suitable configuration for a safe and stable flight. The campaign will provide important information about the optimal battery location and handling qualities. Finally, the design of an attitude and velocity control system will follow with the experiments in order to stabilize the rotorcraft and improve maneuverability.

Authors contacts:

Francesco Mazzeo, francesco.mazzeo@unimore.com , Via P.Vivarelli, 10, Modena (MO), 41125, Italy

Daniele Fattizzo, daniele.fattizzo2@unibo.it , Via Fontanelle, 40, Forlì (FC), 47121, Italy

Giulia Bertolani, giulia.bertolani2@unibo.it , Via Fontanelle, 40, Forlì (FC), 47121, Italy

Emanuele L. de Angelis, emanuele.deangelis4@unibo.it , Via Fontanelle, 40, Forlì (FC), 47121, Italy

Fabrizio Giulietti, fabrizio.giulietti@unibo.it , Via Fontanelle, 40, Forlì (FC), 47121, Italy

Francesco Leali, fleali@unimore.it , Via P.Vivarelli, 10, Modena (MO), 41125, Italy

Marilena D. Pavel, m.d.pavel@tudelft.nl , Kluyverweg 1, Delft, 2629HS, The Netherlands

Appendix A

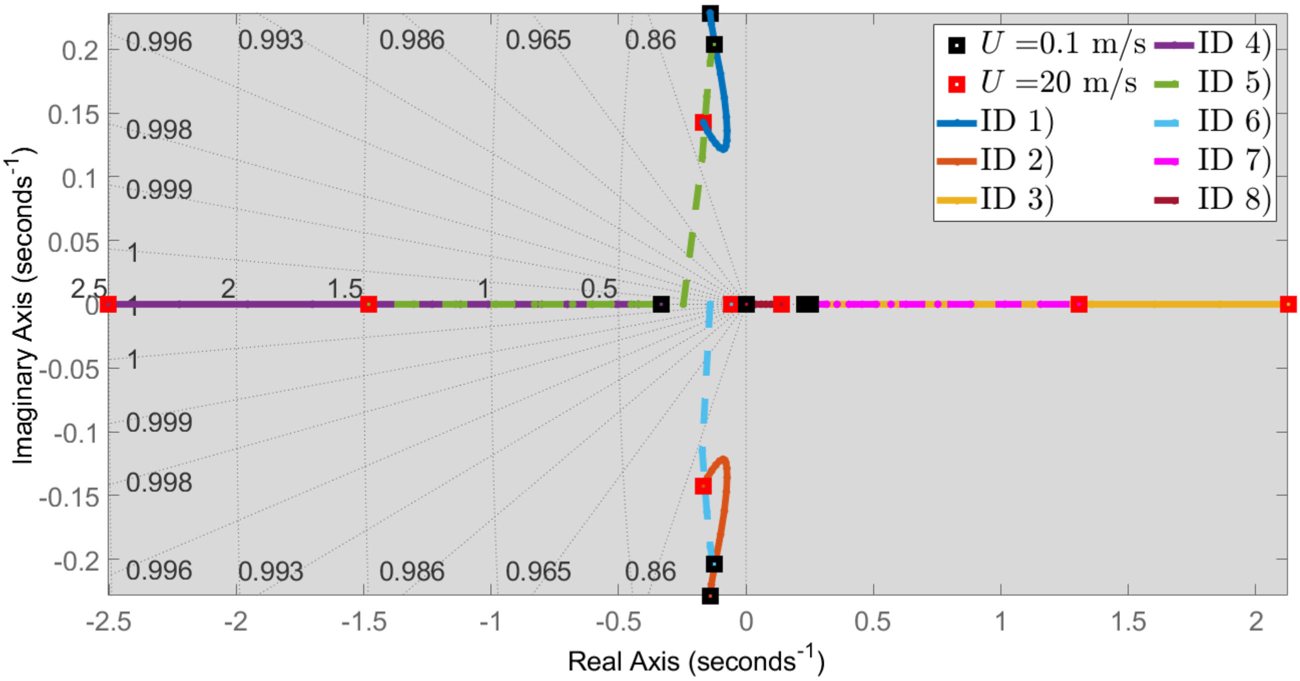

Figure 14: Plot of the poles at variable forward speed. The solid and dashed lines represent, respectively, the evolution of the longitudinal and lateral poles at variable forward speeds. The black/red squares indicate the initial (hovering) and final ($U = 20$ m/s) point.

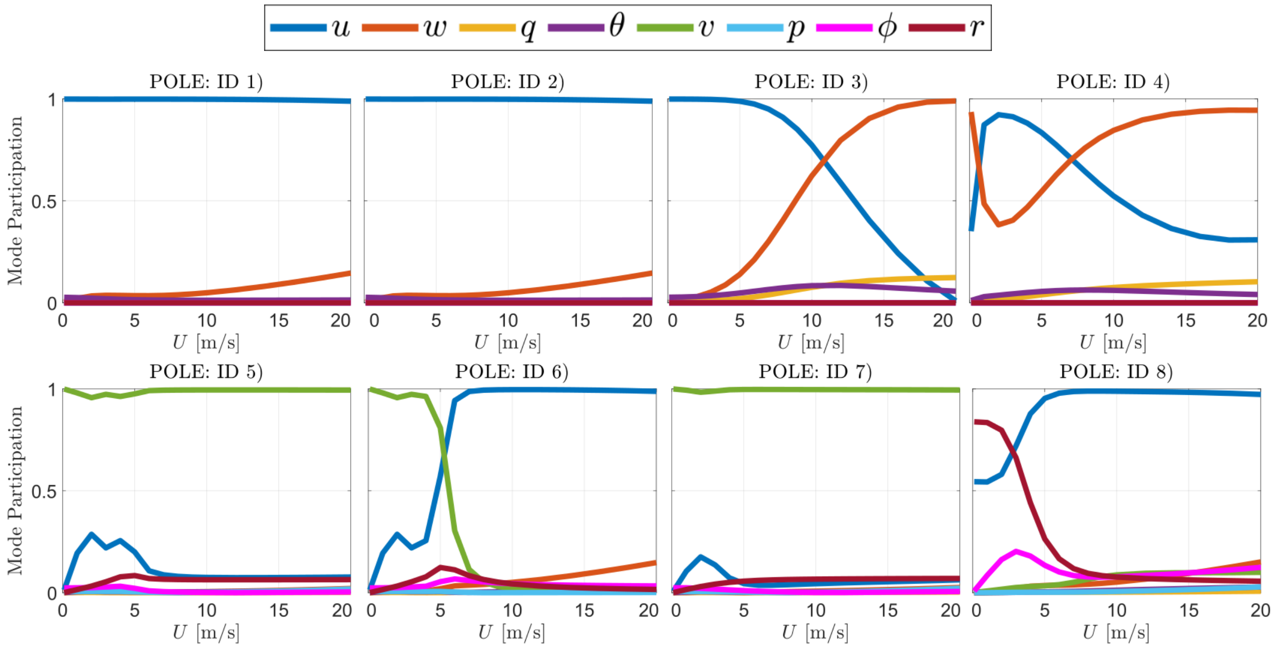

Figure 15: Plot of the participation of each mode for each eigenvalue

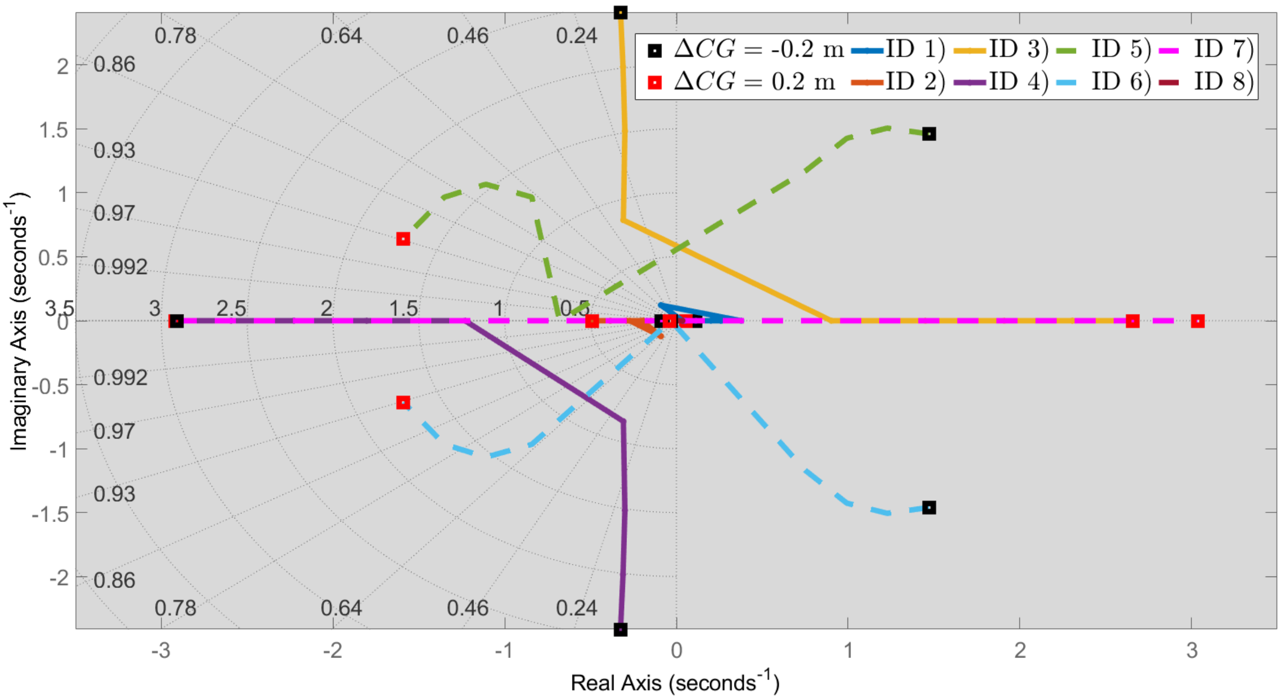

Figure 16: Plot of the poles at $U = 10$ m/s and variable CG position. The solid and dashed lines represent, respectively, the evolution of the longitudinal and lateral poles at variable forward speeds. The black/red squares indicate the initial ($\Delta CG = -0.2$ m) and final ($\Delta CG = 0.2$ m) locations.

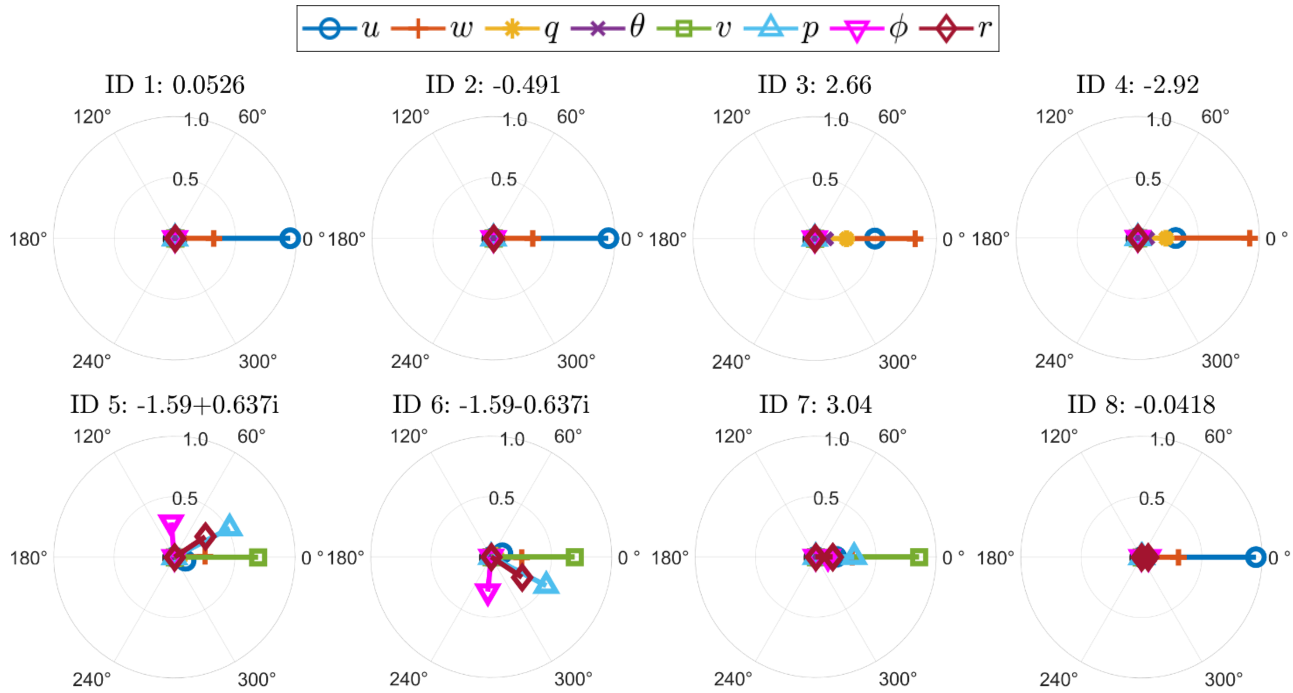

Figure 17: Polar plot of the eigenvectors at $U = 10$ m/s and $\Delta CG = 0.2$ m

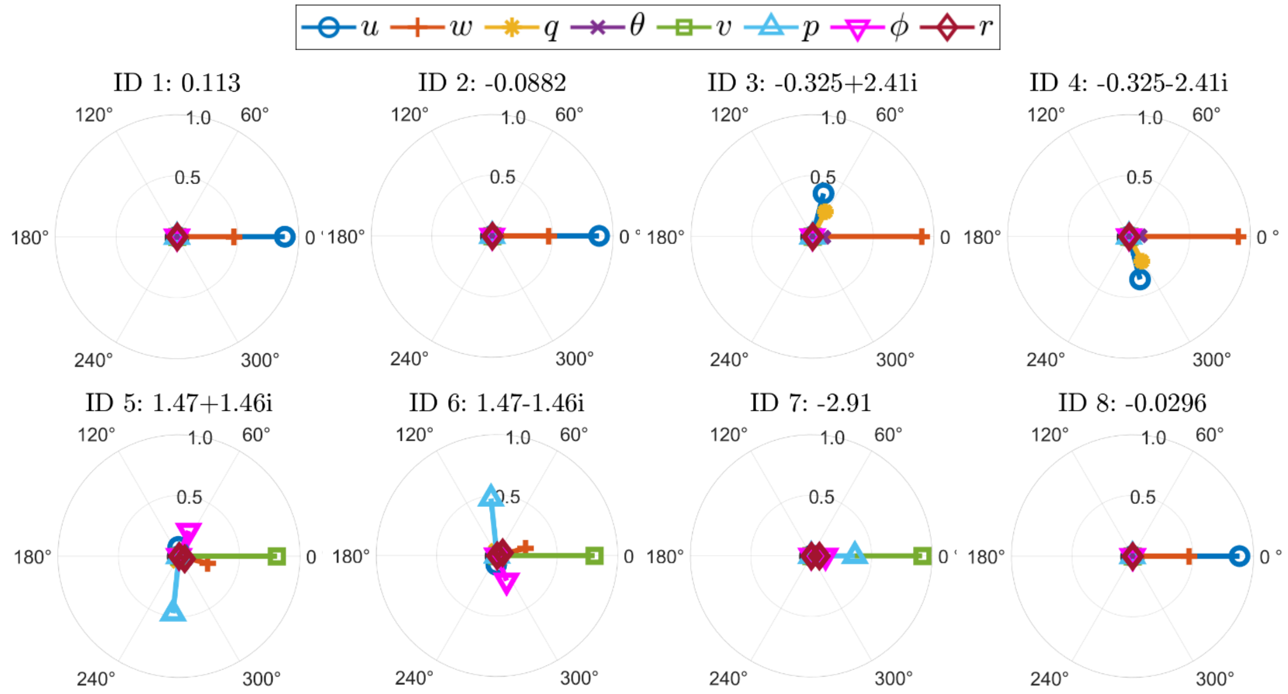

Figure 18: Polar plot of the eigenvectors at $U = 10$ m/s and $\Delta CG = -0.2$ m

REFERENCES

[1] «CO2 Emissions in 2022 – Analysis», *IEA*. https://www.iea.org/reports/co2-emissions-in-2022 (consultato 10 luglio 2023).

[2] H. Ritchie, M. Roser, e P. Rosado, «CO_2 and Greenhouse Gas Emissions», *Our World Data*, mag. 2020, Consultato: 10 luglio 2023. [Online]. Disponibile su: https://ourworldindata.org/emissions-by-sector

[3] R. Goyal *et al.*, «Urban Air Mobility (UAM) Market Study», HQ-E-DAA-TN65181, nov. 2018. Consultato: 10 luglio 2023. [Online]. Disponibile su: https://ntrs.nasa.gov/citations/20190001472

[4] R. Rothfeld, M. Fu, M. Balać, e C. Antoniou, «Potential Urban Air Mobility Travel Time Savings: An Exploratory Analysis of Munich, Paris, and San Francisco», *Sustainability*, vol. 13, fasc. 4, Art. fasc. 4, gen. 2021, doi: 10.3390/su13042217.

[5] R. Rothfeld, A. Straubinger, M. Fu, C. Al Haddad, e C. Antoniou, «Chapter 13 - Urban air mobility», in *Demand for Emerging Transportation Systems*, C. Antoniou, D. Efthymiou, e E. Chaniotakis, A c. di, Elsevier, 2020, pp. 267–284. doi: 10.1016/B978-0-12-815018-4.00013-9.

[6] C. Al Haddad, E. Chaniotakis, A. Straubinger, K. Plötner, e C. Antoniou, «Factors affecting the adoption and use of urban air mobility», *Transp. Res. Part Policy Pract.*, vol. 132, pp. 696–712, feb. 2020, doi: 10.1016/j.tra.2019.12.020.

[7] C. Silva, W. R. Johnson, E. Solis, M. D. Patterson, e K. R. Antcliff, «VTOL Urban Air Mobility Concept Vehicles for Technology Development», in *2018 Aviation Technology, Integration, and Operations Conference*, American Institute of Aeronautics and Astronautics. doi: 10.2514/6.2018-3847.

[8] W. Johnson, C. Silva, e E. Solis, «Concept Vehicles for VTOL Air Taxi Operations», presentato al AHS Specialists'' Conference on Aeromechanics Design for Transformative Vertical Flight, San Francisco, CA, gen. 2018. Consultato: 10 febbraio 2023. [Online]. Disponibile su: https://ntrs.nasa.gov/citations/20180003381

[9] Z. J. Chen, K. A. Stol, e P. J. Richards, «Preliminary design of multirotor UAVs with tilted-rotors for improved disturbance rejection capability», *Aerosp. Sci. Technol.*, vol. 92, pp. 635–643, set. 2019, doi: 10.1016/j.ast.2019.06.038.

[10] H. D. Yoo e S. M. Chankov, «Drone-delivery Using Autonomous Mobility: An Innovative Approach to Future Last-mile Delivery Problems», in *2018 IEEE International Conference on Industrial Engineering and Engineering Management (IEEM)*, dic. 2018, pp. 1216–1220. doi: 10.1109/IEEM.2018.8607829.

[11] M. D. Pavel, «Understanding the control characteristics of electric vertical take-off and landing (eVTOL) aircraft for urban air mobility», *Aerosp. Sci. Technol.*, vol. 125, p. 107143, giu. 2022, doi: 10.1016/j.ast.2021.107143.

[12] W. Johnson e C. Silva, «Observations from Exploration of VTOL Urban Air Mobility Designs», presentato al Asian/Australian Rotorcraft Forum (ARF 2018), Jeju Island, ott. 2018. Consultato: 10 luglio 2023. [Online]. Disponibile su: https://ntrs.nasa.gov/citations/20180007847

[13] S. Yanguo e W. Huanjin, «Design of Flight Control System for a Small Unmanned Tilt Rotor Aircraft», *Chin. J. Aeronaut.*, vol. 22, fasc. 3, pp. 250–256, giu. 2009, doi: 10.1016/S1000-9361(08)60095-3.

[14] X. Wang e L. Cai, «Mathematical modeling and control of a tilt-rotor aircraft», *Aerosp. Sci. Technol.*, vol. 47, pp. 473–492, dic. 2015, doi: 10.1016/j.ast.2015.10.012.

[15] W. Su, S. Qu, G. Zhu, S. S.-M. Swei, M. Hashimoto, e T. Zeng, «Modeling and control of a class of urban air mobility tiltrotor aircraft», *Aerosp. Sci. Technol.*, vol. 124, p. 107561, mag. 2022, doi: 10.1016/j.ast.2022.107561.

[16] J. F. Tan, T. Y. Zhou, Y. M. Sun, e G. N. Barakos, «Numerical investigation of the aerodynamic interaction between a tiltrotor and a tandem rotor during shipboard operations», *Aerosp. Sci. Technol.*, vol. 87, pp. 62–72, apr. 2019, doi: 10.1016/j.ast.2019.02.005.

[17] A. Bacchini, E. Cestino, B. Van Magill, e D. Verstraete, «Impact of lift propeller drag on the performance of eVTOL lift+cruise aircraft», *Aerosp. Sci. Technol.*, vol. 109, p. 106429, feb. 2021, doi: 10.1016/j.ast.2020.106429.

[18] W. Johnson, *Helicopter Theory*. Courier Corporation, 2012.

[19] M. Ishitobi, M. Nishi, e K. Nakasaki, «Nonlinear adaptive model following control for a 3-DOF tandem-rotor model helicopter», *Control Eng. Pract.*, vol. 18, fasc. 8, pp. 936–943, ago. 2010, doi: 10.1016/j.conengprac.2010.03.017.

[20] J. M. A. Peña, S. A. R. Paredes, J. S. V. Martínez, e Y. Aguilar-Molina, «A Laboratory Prototype Tandem Helicopter With Two Degrees of Freedom», *IEEE Access*, vol. 9, pp. 39618–39625, 2021, doi: 10.1109/ACCESS.2021.3064568.

[21] J. L. Williams, *Directional Stability Characteristics of Two Types of Tandem Helicopter Fuselage Models*. National Advisory Committee for Aeronautics, 1954.

[22] Y. Cao, G. Li, e Q. Yang, «Studies of trims, stability, controllability, and some flying qualities of a tandem rotor helicopter», *Proc. Inst. Mech. Eng. Part G J. Aerosp. Eng.*, vol. 223, fasc. 2, pp. 171–177, feb. 2009, doi: 10.1243/09544100JAERO462.
[23] R. F. Stengel, J. R. Broussard, e P. W. Berry, «Digital flight control design for a tandem-rotor helicopter», *Automatica*, vol. 14, fasc. 4, pp. 301–312, lug. 1978, doi: 10.1016/0005-1098(78)90030-4.
[24] A. Dzul, T. Hamel, e R. Lozano, «NONLINEAR CONTROL FOR A TANDEM ROTOR HELICOPTER», *IFAC Proc. Vol.*, vol. 35, fasc. 1, pp. 229–234, gen. 2002, doi: 10.3182/20020721-6-ES-1901.01263.
[25] S. Newman, «The helicopter – efficiency or efficacy?», *Aircr. Eng. Aerosp. Technol.*, vol. 78, fasc. 1, pp. 15–19, gen. 2006, doi: 10.1108/17488840610639636.
[26] M. Rao, S. K. Biswas, B. P. Butz, e D. G. Miller, «Dynamic modeling and feedback control of a side-by-side tandem helicopter», in *Proceedings. 5th IEEE International Symposium on Intelligent Control 1990*, set. 1990, pp. 780–785 vol.2. doi: 10.1109/ISIC.1990.128546.
[27] W. Rhee, L. Myers, e D. McLaughlin, «Aeroacoustics of Vertical Lift Ducted Rotors», in *15th AIAA/CEAS Aeroacoustics Conference (30th AIAA Aeroacoustics Conference)*, American Institute of Aeronautics and Astronautics. doi: 10.2514/6.2009-3333.
[28] J. Sagaga e S. Lee, *Acoustic Predictions for the Side-by-Side Air Taxi Rotor in Hover*. 2021. doi: 10.4050/F-0077-2021-16695.
[29] U. U. the Hood, «Fast-Forwarding to a Future of On-Demand Urban Air Transportation», *Medium*, 27 ottobre 2016. https://uberpubpolicy.medium.com/fast-forwarding-to-a-future-of-on-demand-urban-air-transportation-f6ad36950ffa (consultato 4 luglio 2023).
[30] F. Yunus, D. Casalino, F. Avallone, e D. Ragni, «Efficient prediction of urban air mobility noise in a vertiport environment», *Aerosp. Sci. Technol.*, vol. 139, p. 108410, ago. 2023, doi: 10.1016/j.ast.2023.108410.
[31] M. Barbarino, F. Petrosino, e A. Visingardi, «A high-fidelity aeroacoustic simulation of a VTOL aircraft in an urban air mobility scenario», *Aerosp. Sci. Technol.*, vol. 125, p. 107104, giu. 2022, doi: 10.1016/j.ast.2021.107104.
[32] «Full Report - Study on the societal acceptance of Urban Air Mobility in Europe», *EASA*. https://www.easa.europa.eu/en/full-report-study-societal-acceptance-urban-air-mobility-europe (consultato 27 marzo 2023).
[33] C. Y. Huang, R. Celi, e I. Shih, «Reconfigurable Flight Control Systems for a Tandem Rotor Helicopter», *J. Am. Helicopter Soc.*, vol. 44, fasc. 1, pp. 50–62, gen. 1999, doi: 10.4050/JAHS.44.50.
[34] P. D. Talbot, B. E. Tinling, W. A. Decker, e R. T. N. Chen, «A mathematical model of a single main rotor helicopter for piloted simulation», NAS 1.15:84281, set. 1982. Consultato: 10 febbraio 2023. [Online]. Disponibile su: https://ntrs.nasa.gov/citations/19830001781
[35] H. S. Choi, E. T. Kim, D. I. You, e H. Shim, «Improvements in Small-scale Helicopter Rotor Modeling for the Real-time Simulation of Hovering Flight», *Trans. Jpn. Soc. Aeronaut. Space Sci.*, vol. 54, fasc. 185+186, pp. 229–237, 2011, doi: 10.2322/tjsass.54.229.
[36] G. D. Padfield, *Helicopter Flight Dynamics: The Theory and Application of Flying Qualities and Simulation Modelling*. John Wiley & Sons, 2008.
[37] R. T. N. Chen, «A simplified rotor system mathematical model for piloted flight dynamics simulation», NASA-TM-78575, mag. 1979. Consultato: 10 febbraio 2023. [Online]. Disponibile su: https://ntrs.nasa.gov/citations/19790015806
[38] R. T. N. Chen, «Effects of primary rotor parameters on flapping dynamics». 1 gennaio 1980. Consultato: 10 febbraio 2023. [Online]. Disponibile su: https://ntrs.nasa.gov/citations/19800006879
[39] I. H. Abbott e A. E. V. Doenhoff, *Theory of Wing Sections, Including a Summary of Airfoil Data*. Dover Publications, 1959.
[40] L. A. Viterna e D. C. Janetzke, «Theoretical and experimental power from large horizontal-axis wind turbines», set. 1982, doi: 10.2172/6763041.
[41] W. Kruger, «On Wind Tunnel Tests and Computations Concerning the Problem of Shrouded Propellers», NACA-TM-1202, feb. 1949. Consultato: 12 giugno 2023. [Online]. Disponibile su: https://ntrs.nasa.gov/citations/20050241797
[42] G. J. Leishman, *Principles of Helicopter Aerodynamics*. Cambridge University Press, 2006.
[43] B. G. Jimenez e R. Singh, «Effect of Duct-Rotor Aerodynamic Interactions on Blade Design for Hover and Axial Flight», in *53rd AIAA Aerospace Sciences Meeting*, American Institute of Aeronautics and Astronautics. doi: 10.2514/6.2015-1030.
[44] A. I. Abrego, R. W. Bulaga, e M. Rutkowski, «Performance Study of a Ducted Fan System», 1 gennaio 2002. Consultato: 10 luglio 2023. [Online]. Disponibile su: https://ntrs.nasa.gov/citations/20020052231
[45] B. N. Bourtsev e S. V. Selemenev, «Fan – in – Fin Performance at Hover Computational Method».

Acknowledgments
The authors acknowledge and thank the company SAB Group S.R.L. for providing the rotorcraft's prototype and sharing constructive data. This study was carried out within the MOST - Sustainable Mobility National Research Center and received funding from the European Union Next-GenerationEU (PIANO NAZIONALE DI RIPRESA E RESILIENZA (PNRR) - MISSIONE 4 COMPONENTE 2, INVESTIMENTO 1.4 - D.D. 1033 17/06/2022, CN00000023). This manuscript reflects only the authors' views and opinions, neither the European Union nor the European Commission can be considered responsible for them.